

Article

Geometrical Calibration of a 2.5D Periapical Radiography System

Che-Wei Liao ¹, Ming-Tzu Tsai ², Heng-Li Huang ^{3,4}, Lih-Jyh Fuh ^{3,5} , Yen-Lin Liu ⁶,
Zhi-Teng Su ³ and Jui-Ting Hsu ^{3,4,*} 

¹ Graduate Institute of Biomedical Sciences, China Medical University, Taichung 404, Taiwan; z88318831@gmail.com

² Department of Biomedical Engineering, Hungkuang University, Taichung 433, Taiwan; anniemtt@sunrise.hk.edu.tw

³ School of Dentistry, College of Dentistry, China Medical University, Taichung 404, Taiwan; hlhuang@mail.cmu.edu.tw (H.-L.H.); ljfuh@mail.cmu.edu.tw (L.-J.F.); u106000016@cmu.edu.tw (Z.-T.S.)

⁴ Department of Bioinformatics and Medical Engineering, Asia University, Taichung 413, Taiwan

⁵ Department of Dentistry, China Medical University and Hospital, Taichung 404, Taiwan

⁶ Department of Biomedical Imaging and Radiological Science, China Medical University, Taichung 404, Taiwan; u105020002@cmu.edu.tw

* Correspondence: jthsu@mail.cmu.edu.tw; Tel.: +886-4-2205-3366 (ext. 2308)

Received: 30 December 2019; Accepted: 27 January 2020; Published: 30 January 2020



Abstract: The objective of this study was to develop a geometrical calibration method applicable to the 2.5D prototype Periapical Radiography System and estimate component position errors. A two-steel-ball phantom with a precisely known position was placed in front of a digital X-ray sensor for two-stage calibration. In the first stage, the following three parameters were estimated: (1) r , the distance between the focal spot and the rotation axis of the X-ray tube; (2) ψ , the included angle between the straight line formed by the X-ray tube's focal spot and rotation axis and the straight line of the orthogonal sensor; and (3) L_4 , the distance between the rotation axis and the plane where the two steel balls were positioned. In the second stage, the steel balls' positions were determined to calculate the positions of the X-ray tube on the x , y , and z axes. Computer simulation was used to verify the accuracy of the calibration method. The results indicate that for the calibration approach proposed in this study, the differences between the estimated errors and setting errors were smaller than 0.15% in the first and second stages, which is highly accurate, verifying its applicability to accurate calibration of the 2.5D Periapical Radiography System.

Keywords: geometric calibration; periapical radiography; computed tomosynthesis; quasi-3D imaging; 2.5D

1. Introduction

The application of X-ray radiography in clinical dentistry is prevalent. Currently, dental radiographic images can be divided into 2D and 3D radiographic images, and 2D radiographs can be further divided into intraoral and extraoral. Equipment for capturing intraoral radiographs includes periapical, bitewing, and occlusal films, whereas that for extraoral radiographs includes panoramic and cephalometric films. The most substantial problem related to 2D radiographs is the superposition of tissue images, which leads to dentists being unable to accurately determine the solid forms of teeth or bone structures [1,2]. The commonest form of 3D radiography is cone beam computed tomography (CBCT). This technique has the advantages of enabling 3D image developments in diagnosis, giving doctors more information related to the structures and forms of interior tissues at different depths [3]. However, CBCT image resolution can only reach a maximum of 70 μm [4,5].

This resolution is beneficial for examining patients with mandible fracture, nasal cavity, and tooth impaction, as well as for conducting preoperative planning of dental implant surgery. However, lesions such as root microfractures and root fractures are difficult to identify. In recent years, the development of digital periapical radiography has enabled an image resolution of at most 20 μm [6]. This resolution enables clear observation of such lesions. However, the clinical applicability of this approach is still limited in that only 2D images can be captured [7].

To overcome the disadvantage of only providing 2D intraoral periapical film images, the present research team proposed a new piece of equipment, the 2.5D Periapical Radiography System, in 2018 [8]. This device is similar to a CBCT machine, with the most substantial difference being that a digital X-ray sensor is placed inside the patient's oral cavity. The device has a supporting frame for hanging the X-ray tube. During image capture, the tissue is observed on a rotation axis, and the X-ray tube has a limited angle of rotation (e.g., $\pm 30^\circ$). Continuous 2D images of different angles are imported to a computer for image reconstruction using digital tomosynthesis, allowing the reconstructed images of different depths to be observed. Although the prototype of this proposed system can obtain reconstructed images in different depths, the shooting time is over 10 min because current commercially available digital X-ray sensors are unable to continuously shoot at high frame rates, rendering them inapplicable to clinical dentistry [9–11]. Therefore, our team developed a high-frame-rate sensor in 2019 [12]. This sensor can achieve a frame rate of up to 15 Hz, which substantially reduces the shooting time to under 10 s, thus increasing its clinical feasibility. However, artefacts and blurring were observed in images reconstructed using experimental *in vitro* images of teeth because hardware component positioning was not established through accurate geometrical calibration.

Scholars have proposed calibration methods related to computed tomography (CT) and micro-CT [13–16], most of which involve the use of a phantom with known interior geometrical positions for geometrical calibration of the hardware components. Phantoms for calibration are mostly items such as steel balls [15], ruby balls [14], and steel wires [13] covered in resin of a precise size. First, a single- or multi-angle projection is applied to the phantom, and feature points are captured from the obtained 2D images. Next, hardware errors are calculated, and the calculated error values are used to adjust the hardware component positions. Alternatively, the image deviation method is used to remove images that are blurred because hardware components are not installed in ideal positions [17]. However, methods proposed by previous scholars cannot be effectively applied to the 2.5D Periapical Radiography System because of the system's small sensor size and the sensor being too close to the object. Therefore, such previous methods [18–23] are unsuitable for the geometric calibration of the proposed system.

This study proposes an approach for the geometrical calibration of hardware component positioning that is suitable for digital tomosynthesis using small-area sensors with an extremely short distance between the sensor and object. The calibration approach involves using a two-steel-ball phantom with precise known sizes and placing the phantom in front of the sensor. The two steps of the calibration process are conducted separately to calculate the error values of the X-ray tube at the x, y, and z axes. The linking lines of the X-ray tube and rotation axis can intersect orthogonally at the center of the sensor.

2. Materials and Methods

2.1. 2.5D Periapical Radiography System

The 2.5D Periapical Radiography System was introduced in our previous study (Figure 1a) [8]. The system consists of a supporting frame, a dental cone beam X-ray generator (PDM90P, Spellman, Hauppauge, NY, USA), an electric rotating platform (DG130R-AZAAD-3, Taiwan Oriental Motor Co., Ltd., Taipei, Taiwan), and an intraoral digital sensor (RVG6200-SIZE1, Carestream Dental, Stuttgart, Germany). The intraoral digital sensor was fixed onto a specific arm, which connected it to the supporting frame. For computed tomosynthesis, a human tooth was placed in the front right section

of the detector to obtain spatial resolution in three axial directions. Forty-one radiographs were captured in circular scanning geometry with a tomosynthetic angle of $\pm 60^\circ$, and images were acquired every rotation of 3° . First, the 41 images were preprocessed. Then, an analytical method was used to reconstruct images obtained from the computed tomosynthetic approach. The resulting image reconstructed from computed tomosynthesis was a 2.5D image of a tooth in the coronal plane (Figure 1b). All reconstruction algorithms used in this study were implemented in MATLAB 2016 (Mathworks, Natick, MA, USA).

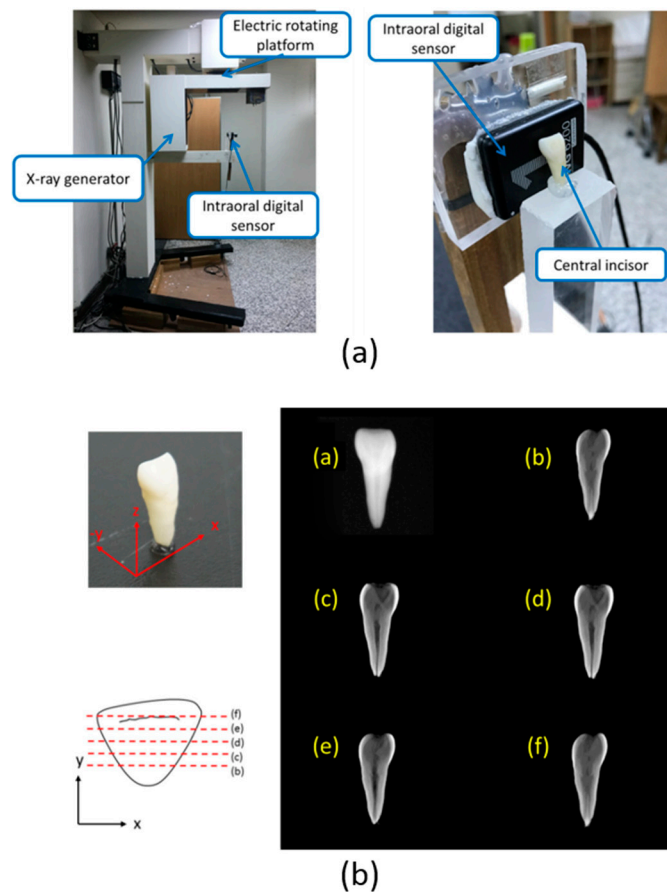
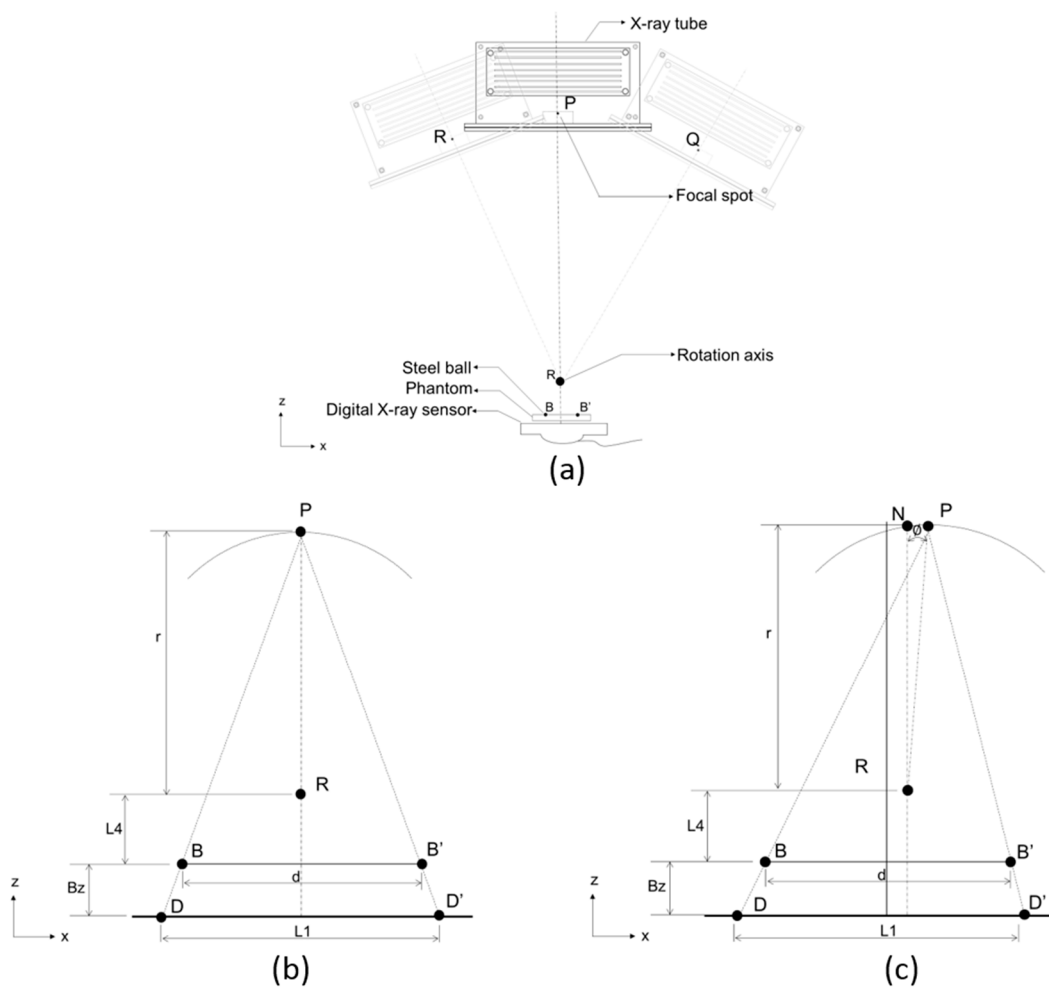


Figure 1. The 2.5D Periapical Radiography System was developed in 2018 [8]. (a) Prototype of the intraoral digital tomosynthesis system. (b) Reconstructed images obtained from the 2.5D prototype of the intraoral digital tomosynthesis system at different distances from the sensor surface.

2.2. Geometric Calibration Algorithm

Ideally, for hardware structures related to digital tomosynthesis, the focal spot of the X-ray tube (Point P) should be perpendicular to and intersect orthogonally with the sensor's center (Figure 2a). In addition, the positions of the focal spot (Point P), rotation axis (Point R), and central axis of the sensor should form a straight line (Figure 2b). The reconstructed images captured using this structure did not contain artefacts resulting from hardware being uncalibrated. However, in real-world settings, the focal spot (Point P) in an uncalibrated system may cause the linked line between points P and R to become non-perpendicular to the sensor, and the linked line between points P and R may not align with the center of the sensor. Such conditions cause artefacts and blurs in the reconstructed images and influence image quality (Figure 2c).



P_{ideal}	Focal point of the X-ray tube at 0° in an ideal system.
R	Rotation axis position.
B	Position of Steel Ball I.
B'	Position of Steel Ball II.
D	Center position of the projection of point B of the phantom on the sensor.
D'	Center position of the projection of point B' of the phantom on the sensor.
P_{real}	Focal Point Position of the X-ray tube at 0° in an actual system.
N	A point on the rotation path of the X-ray tube in an actual system. The linking line of this point and Point R intersects orthogonally with the sensor.
ψ	Included angle between the linking line formed by Point P_{real} and Point R and the straight line orthogonal to the sensor (line \overline{NR}).
r	Distance of the focal spot of the X-ray tube to Point R.
d	Distance between B and B'
L_1	Distance between D and D'
L_4	Distance between the rotation axis position and the phantom.
Bz	Distance between the phantom and the sensor film.

Figure 2. The difference between the ideal hardware position and the actual hardware component position. (a) Major components of the 2.5D Periapical Radiography System. (b) Ideal tomosynthesis geometry (focal spot, Point P; location of the two-steel-ball phantom, B and B'; projection points D and D' of B and B'; rotation axis point R). (c) Real tomosynthesis geometry.

The calibration method proposed in this study is conducted in two steps (Figure 3). In Step I, the focal spot of the X-ray tube is rotated and adjusted so that the linking line between the focal spot and the rotation axis is orthogonal to the sensor. In Step II, the linking line of the focal spot is adjusted so that the rotation axis is orthogonal to the sensor at its center.

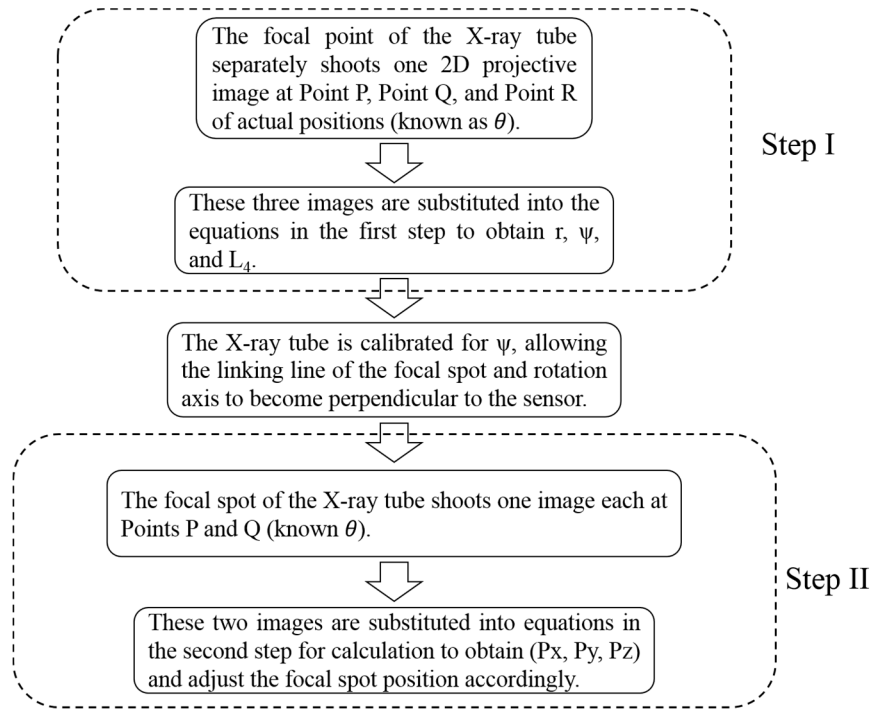


Figure 3. Two-step calibration process. The calibration method proposed in this study is conducted in two steps. In Step I, the focal spot of the X-ray tube is rotated and adjusted so that the linking line between the focal spot and the rotation axis is orthogonal to the sensor. From Step I: parameters r (distance of the focal spot of the X-ray tube to Point R), ψ (included angle between the linking line formed by Point P and Point R and the straight line orthogonal to the sensor), and L_4 (distance between the rotation axis position and the phantom) can be calculated. In Step II, the linking line of the focal spot is adjusted so that the rotation axis is orthogonal to the sensor at its center. From Step II: parameters P_x (focal spot x-coordinate value), P_y (focal spot y-coordinate value), and P_z (focal spot z-coordinate value) can then also be calculated.

Step I (Figure 4) calculates the distance (r) between the focal spot of the X-ray tube (Point P) and the rotation axis of the X-ray tube's rotation structure, the angle (ψ) between the linking line of the focal spot (Point P) and rotation axis (Point R) and the straight line orthogonal to the sensor (\overline{NR}), and the distance (L_4) between the rotation axis (Point R) and the linking line between the two steel balls of the phantom. This calibration method requires a two-steel-ball phantom of known precise sizes, and the distance between the two steel balls (d) must be known. The two-steel-ball phantom is appressed to the sensor (B_z and $B_{z'}$ are known), and the X-ray tube's focal spot shoots one 2D image at Point P (Figure 4a) with the projective distance of the phantom to the sensor calculated as $L_1 (= \overline{DD'})$. Then, we rotate for angle $\pm\theta$ (θ can be any value less than 60° except 0° , while 30° is recommended—if θ is larger than 60° , the projection of the steel ball will fall outside the sensor range) and move the X-ray tube to Point Q (Figure 4b) and Point R (Figure 4c) to shoot one 2D image each with the projective distance of the phantom on the sensor as $L_2 (= \overline{DD'})$ and $L_3 (= \overline{DD'})$. L_1 , L_2 , and L_3 can be calculated from the 2D images and the actual resolution size of the sensor. Finally, we substitute the known parameters B_z , $B_{z'}$, θ , d , L_1 , L_2 , and L_3 into the derived equations as follows. Parameters r , ψ , and L_4 can then be calculated.

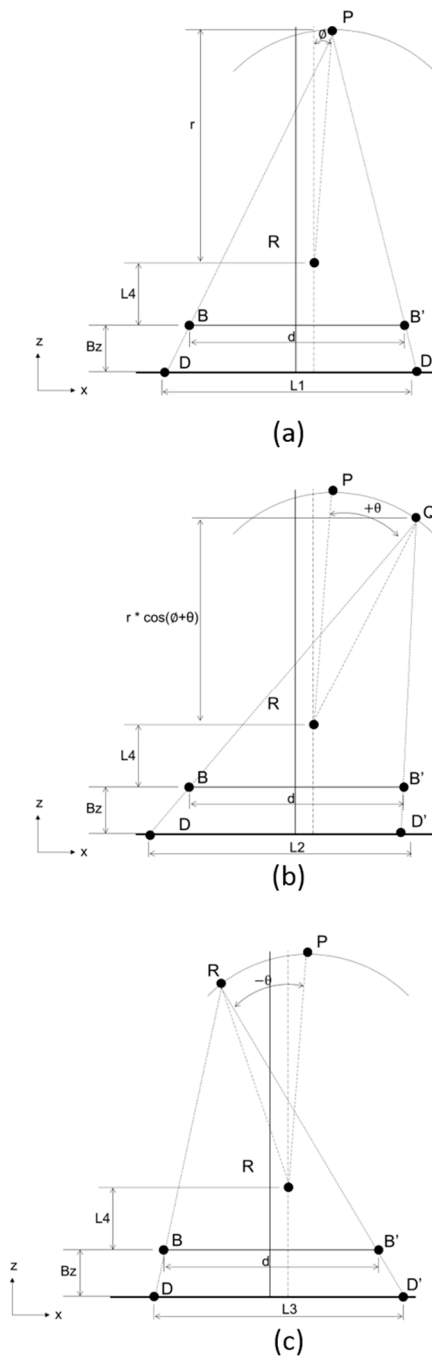


Figure 4. Flow chart of Step I. Step I calculates the distance (r) between the focal spot of the X-ray tube (Point P) and the rotation axis of the X-ray tube’s rotation structure, the angle (ψ) between the linking line of the focal spot (Point P) and rotation axis (\overline{PR}) and the straight line orthogonal to the sensor, and the distance (L_4) between the rotation axis (Point R) and the linking line between the two steel balls of the phantom: (a) The actual hardware positions directly after assembly; (b) the X-ray tube’s focal spot rotates $+\theta^\circ$; (c) the X-ray tube’s focal spot rotates $-\theta^\circ$. P is the position of the focal spot, R is the position of the rotation axis, B and B’ are the positions of the two steel balls on the phantom, and D and D’ are the positions of the projections of the two steel balls on the sensor.

(See Appendix A for a more detailed derivation about step I.)

Before Step II is conducted, we rotate the X-ray tube by $-\psi^\circ$ (calculated from Step I): specifically, we adjust the focal spot to the position in which its linking line with the rotation axis is orthogonal to the sensor (Figure 5).

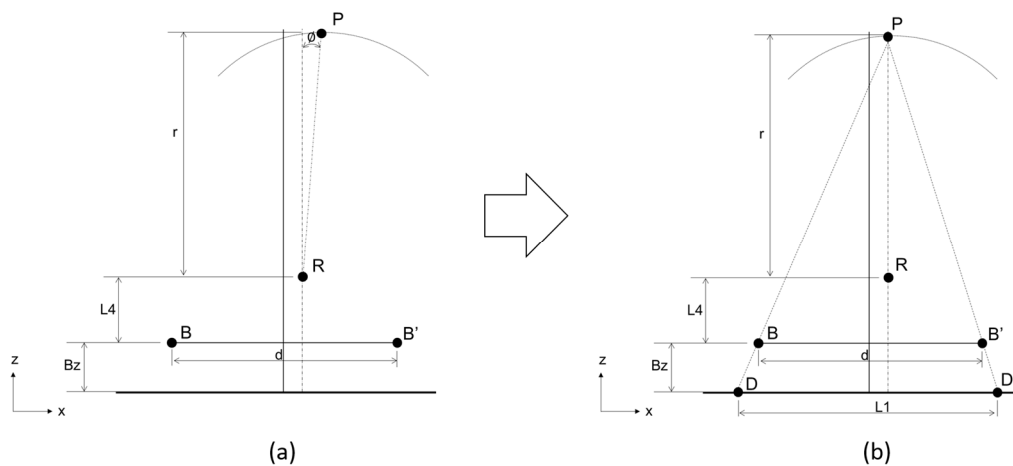


Figure 5. Before Step II is conducted, we rotate the X-ray tube by $-\psi^\circ$ (calculated from step I): specifically, we adjust the focal spot to the position in which its linking line with the rotation axis is orthogonal to the sensor. **(a)** Original position of the X-ray tube. First, rotate the X-ray tube by $-\psi^\circ$ (calculated from Step I). **(b)** Hardware positions after adjustment. The focal spot is adjusted to where its linking line with the rotation axis is orthogonal to the sensor.

Then, we employ Step II (Figure 6) to calculate the deviational distances (P_x , P_y , and P_z) on the x , y , and z axes of Point P away from the center of the sensor. Similarly, the two-steel-ball phantom is appressed to the sensor, and the X-ray tube shoots one 2D image at Point P (Figure 6a) with the projective distance of the phantom on the sensor as $L_1 (= \overline{DD'})$. Then, the X-ray tube is rotated by θ° (θ can be any value less than 60° except 0° , while 30° is recommended) and moved from Point P to Q (Figure 6b) in order to shoot another 2D image, with the projective distance of the phantom on the sensor being $L_2 (= \overline{CC'})$. We substitute the known parameters B_y , $B_{y'}$, L_1 , L_2 , d , and r into the derived equations described as follows to calculate the three parameters P_x , P_y , and P_z , which are the error values between the focal spot and the ideal position. In addition, $P_z + r + L_4 + B_z$ is the distance between the focal spot and the sensor.

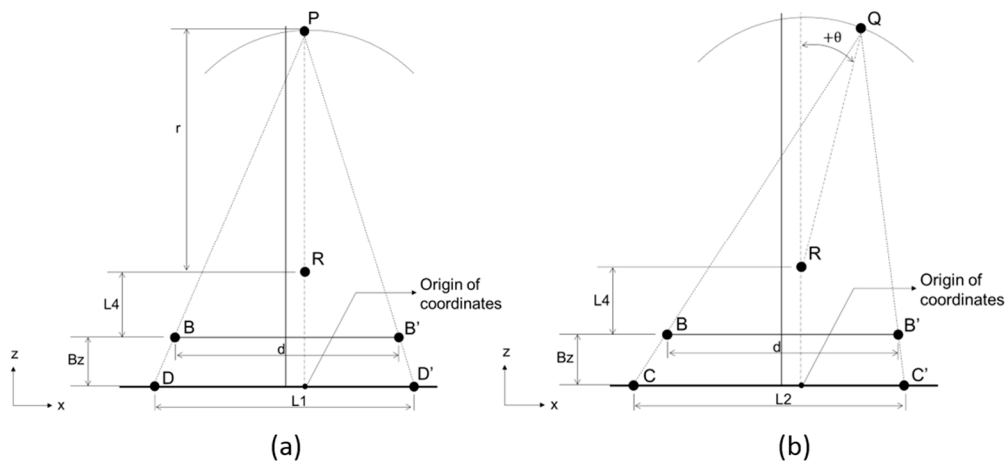


Figure 6. Flow chart of Step II. Step II is used to calculate the deviational distances (P_x , P_y , and P_z) on the x , y , and z axes of Point P away from the center of the sensor. First the X-ray tube is at Point P to shoot a 2D image, then moved from Point P to Q in order to shoot another 2D image. **(a)** Point P after the calibration in Step I. **(b)** Focal point rotates $+\theta^\circ$.

(See Appendix A for a more detailed derivation about step II.)

3. Results

Numerical simulations were used to verify the accuracy of this calibration method, and SolidWorks 2016 (Dassault Systemes SolidWorks Corporation, Commonwealth of Massachusetts, USA) was used to verify the simulation accuracy. The desired positions of each component and error values could be precisely set in the 3D coordinates of SolidWorks. Then, the position parameters of the phantom’s projection on the digital X-ray sensor could be obtained. Finally, these position parameters were substituted into the calibration method proposed in this study to verify its accuracy and feasibility; this involved calculating whether the calculated error and the setting error are identical.

The calibration method proposed in this study involves two steps; hence, the computer simulation was divided into two stages as well. The parameters calibrated in Step I were R , ψ , and L_4 . Table 1 lists the five setting errors for computer simulation. The calculation errors from Step I and the self-established errors were determined to be $< 0.015\%$.

Table 1. Calibration results of the three parameters obtained from Step I.

Test Number	L_4 (mm)			ψ (°)			r (mm)		
	Ideal	Estimate	Error (%)	Ideal	Estimate	Error (%)	Ideal	Estimate	Error (%)
1	5.0	5.00004399	0.00088	3.0	3.00034641	0.01155	335	335.000001	0.00000
2	6.5	6.499985761	-0.00022	2.8	2.79995015	-0.00178	332	331.5000007	0.00000
3	4.1	4.100159545	0.00389	3.7	3.70041803	0.01130	337	337.2999967	0.00000
4	5.3	5.300042976	0.00081	1.3	1.300326732	0.02513	334	333.8000022	0.00000
5	4.2	4.199978173	-0.00052	5.9	5.899961593	-0.00065	333	332.6999966	0.00000

The proposed calibration method involves two steps; hence, the simulation in the computer was divided into two stages as well. The parameters calibrated in Step II were Pz , $B'x$, $B'y$, Bx , By , Px , and Py . Table 2 lists the five setting errors for computer simulation. The errors of calculation determined from Step II and the self-established errors were all smaller than 0.01% .

Table 2. Calibration results of the parameters obtained from Step II.

Group 1			
Parameter	Ideal	Estimate	Error (%)
Pz	350	350.000001	0.00000
$B'x$	-12.1756613	-12.1756622	0.00001
$B'y$	1.6572935	1.6572934	-0.00001
Bx	7.8076613	7.8076605	-0.00001
By	0.8407065	0.8407063	-0.00002
Px	-2.438	-2.4380285	0.00117
Py	6.892	6.8919944	-0.00008
Group 2			
Parameter	Ideal	Estimate	Error (%)
Pz	350	349.999999	0.00000
$B'x$	9.25091935	9.25091994	0.00001
$B'y$	-0.13745354	-0.1374539	0.00026
Bx	-10.7109194	-10.7109188	-0.00001
By	1.09745354	1.09745319	-0.00003
Px	-0.54	-0.5399793	-0.00383
Py	0.19	0.1899876	-0.00653

Table 2. Cont.

Group 3			
Parameter	Ideal	Estimate	Error (%)
Pz	350	350.000001	0.00000
B'x	-12.1756613	-12.1756622	0.00001
B'y	1.65729352	1.65729336	-0.00001
Bx	7.80766134	7.80766052	-0.00001
By	0.84070648	0.84070632	-0.00002
Px	-2.438	-2.43802854	0.00117
Py	6.892	6.8919944	-0.00008
Group 4			
Parameter	Ideal	Estimate	Error (%)
Pz	370.83	370.829997	0.00000
B'x	9.25091935	9.25092049	0.00001
B'y	-0.13745354	-0.13745374	0.00015
Bx	-10.7109194	-10.7109182	-0.00001
By	1.09745354	1.09745334	-0.00002
Px	-0.54	-0.53995807	-0.00776
Py	0.19	0.18999275	-0.00382
Group 5			
Parameter	Ideal	Estimate	Error (%)
Pz	350	349.999997	0.00000
B'x	7.50455987	7.50456092	0.00001
B'y	0.81019259	0.81019316	0.00007
Bx	-12.4845599	-12.4845588	-0.00001
By	1.46980741	1.46980797	0.00004
Px	-2.92	-2.91996328	-0.00126
Py	1.66	1.6600196	0.00118

4. Discussion

According to a joint statement by the American Association of Endodontists and the American Academy of Oral and Maxillofacial Radiology in 2015, the optimal imaging choice for root canal evaluation is intraoral X-ray [24]. Therefore, image quality often influences dentists' diagnosis and treatment methods. The 2D periapical film images commonly used in clinics cannot provide sufficient information for dentists due to image superposition limitations. Our team previously developed a 2.5D Periapical Radiography System but failed to obtain clear images because of limitations in the accurate adjustment of hardware positions. However, the calibration methods for CT cannot be applied to the 2.5D Periapical Radiography System. Therefore, in this study we proposed a two-step calibration method that enables the linking line of the X-ray tube and rotation axis to intersect orthogonally with the sensor's center point. This calibration method can be applied to a machine with medium or large sensors in digital tomosynthesis systems in the future.

Several studies have applied digital tomosynthesis to dentistry [25–32], but it has not been widely applied to clinical use due to the limits of the technology at this time. Our team proposed the 2.5D Periapical Radiography System in 2018 [8] and developed a high-frame-rate sensor. This device enables placing a digital X-ray sensor in the mouth of a patient and can reconstruct images in different depths using shots at limited angles. However, during shooting, the research team discovered that the imaging speed of all commercially available digital X-ray sensors excluded their application to the developed system. Using commercial digital X-ray sensors results in excessively long shooting times unsuitable for practical clinical applications. The long shooting time not only causes discomfort for patients but also generates artefacts in the reconstructed images due to natural breathing motions or unconscious tiny swings of patients during shooting. Therefore, our team also developed a high-frame-rate intraoral

periapical sensor [12] which can reach a shooting speed of 15 Hz and reduce the shooting time to within 10 s.

CT and digital tomosynthesis systems require accurate calibration of main hardware component positions; otherwise, errors in the hardware component positions will generate artefacts in the reconstructed images. The literature related to hardware position calibration for CT or micro-CT [14,15,33,34] indicates that phantoms can be used to calibrate 5 to 11 hardware position error parameters [14], with the 7 most common presented as follows: (1) sensor offset along the x axis, (2) sensor offset along the y axis, (3) angle of sensor tilted around the x axis, (4) angle of sensor tilted around the y axis, (5) angle of sensor tilted around the z axis, (6) perpendicular distance from the digital X-ray sensor to the rotation axis, and (7) perpendicular distance from the rotation axis to the X-ray tube. Numerous scholars have used phantoms to calibrate the hardware positions of CT or micro-CT instruments [32,33]. Calibration can be divided into two types, single- and multi-angle projection. Various scholars have proposed multiprojection calibration using 12 or 6 [35] steel balls to form two-ring phantoms. Sun [34] and Zhao [14] have proposed single projection methods using four- and nine-point phantoms to determine component position errors. However, these calibration methods for CT or micro-CT cannot be applied to the 2.5D Periapical Radiography System. The major problem is that the system shoots using digital tomosynthesis with stationary sensors and objects, which differ from those used in CT or micro-CT.

Currently, digital breast tomosynthesis is the commonest digital tomosynthesis approach used in clinical settings. In 2003, General Electric Company proposed a patent for geometrical calibration that applies to breast tomosynthesis [36]. In laboratory settings, researchers have also attempted calibration using two-ring phantoms or five-steel-ball phantoms [35], but these methods are unsuitable for the 2.5D Periapical Radiography System. This is mainly because the area of the digital X-ray sensors used in this system is considerably smaller than those of other systems. In addition, the object (tooth) is extremely close to the sensor; consequently, the magnification level is insufficient for accurately identifying the form and characteristics of the phantoms. For the calibration of digital tomosynthesis systems with small-area digital X-ray sensors, Li also proposed using a two-steel-ball phantom, but this method requires an estimated focal spot position before calibration and calculation can be conducted [19].

In this study, a new digital tomosynthesis method was proposed that involves two-step calibration using a two-steel-ball phantom with known geometrical positions. In the first step, an X-ray tube is used to shoot one 2D X-ray image at three different positions (P, Q, and R) separately. Then, the positions of the two steel balls are captured on the 2D image and substituted into equations to calculate the following three hardware position parameters: (1) the distance r between the focal spot, Point P, and the center of the X-ray tube rotation structure; (2) the included angle ψ between the straight line (\overline{PR}) connected by the focal spot, Point P, and the rotation axis and the straight line (\overline{NR}) that intersects the sensor orthogonally; and (3) the distance L_4 between the rotation axis, Point R, and the linking line of the two steel balls on the phantom. Next, the hardware components are adjusted in accordance with the parameters obtained in Step I before calibration is conducted in Step II. In the second step, the X-ray tube is used to shoot one 2D X-ray image at two positions (P and Q). Then, the positions of the two steel balls on the 2D image are captured and entered into equations to calculate the offsets (P_x , P_y , and P_z) of Point P of the X-ray tube from the sensor center on axes x, y, and z. According to the computer simulation results, the calibration method proposed in this study has extremely high accuracy. The errors of the estimation method from the ideal positions in Steps I and II were smaller than 0.015% and 0.01%, respectively. This method is applicable to digital X-ray sensors in small areas. Applying this method to geometrical calibration for digital tomosynthesis systems in the future will reduce the errors generated in setting up hardware component positions.

Although the calibration method proposed in this study can already accurately calibrate digital tomosynthesis systems, some limitations remain. First, the method cannot be used to calculate the angular errors on the three axes and the position errors of the rotation axis for the digital X-ray sensor. Second, the two-steel-ball phantom used in this study requires extremely accurate information on the

distance between the balls; this is in accordance with most studies that use phantoms for calibration [19]. Third, similar to related studies [34], the method proposed in this study was only verified using computer simulations; it still requires further verification through practical shooting and calibration.

Author Contributions: Conceptualization, C.-W.L. and J.-T.H.; Data curation, M.-T.T., Y.-L.L. and J.-T.H.; Formal analysis, C.-W.L.; Investigation, C.-W.L. and J.-T.H.; Methodology, C.-W.L., H.-L.H., L.-J.F., Y.-L.L., Z.-T.S. and J.-T.H.; Resources, L.-J.F. and J.-T.H.; Supervision, J.-T.H.; Validation, C.-W.L.; Writing—original draft, C.-W.L., M.-T.T., H.-L.H. and J.-T.H.; Writing—review and editing, J.-T.H. All authors have read and agreed to the published version of the manuscript.

Funding: This study was partially supported by China Medical University (CMU108-S-01), Taiwan.

Conflicts of Interest: The authors declare no conflict of interest.

Appendix A

Step I.

$$\frac{(r \cdot \cos\phi + L_4)}{(r \cdot \cos\phi + L_4) + B_z} = \frac{d}{L_1} \tag{A1}$$

$$\frac{r \cdot \cos(\phi + \theta) + L_4}{[r \cdot \cos(\phi + \theta) + L_4] + B_z} = \frac{d}{L_2} \tag{A2}$$

$$\frac{r \cdot \cos(\phi - \theta) + L_4}{[r \cdot \cos(\phi - \theta) + L_4] + B_z} = \frac{d}{L_3} \tag{A3}$$

$$L_4 = \frac{\frac{d \cdot B_z}{L_2 - d} + \frac{d \cdot B_z}{L_3 - d} - \frac{2 \cdot d \cdot B_z \cdot \cos\theta}{L_1 - d}}{2 \cdot (1 - \cos\theta)} \quad (\theta \text{ cannot be zero and must be less than } 90^\circ)$$

$$r = \sqrt{\left(\frac{d \cdot B_z}{L_1 - d} - L_4\right)^2 + \left[\frac{\left(\frac{d \cdot B_z}{L_3 - d} - \left(\frac{d \cdot B_z}{L_2 - d}\right)\right)}{2 \cdot \sin\theta}\right]^2}$$

$$\cos\phi = \frac{\left(\frac{d \cdot B_z}{L_1 - d}\right) - L_4}{r}$$

from (A1),

$$\frac{r \cdot \cos\phi + L_4}{(r \cdot \cos\phi + L_4) + B_z} = \frac{d}{L_1}.$$

from (A2),

$$r \cdot \cos\phi \cdot L_1 + L_1 \cdot L_4 = r \cdot \cos\phi \cdot d + L_4 \cdot d + d \cdot B_z.$$

multiply both sides of the equation by $\frac{L_1}{L_1}$:

$$\frac{r \cdot \cos\phi \cdot L_1 + L_1 \cdot L_4}{r \cdot \cos\phi \cdot L_1 + L_1 \cdot L_4 + L_1 \cdot B_z} = \frac{r \cdot \cos\phi \cdot d + d \cdot L_4 + d \cdot B_z}{r \cdot \cos\phi \cdot L_1 + L_1 \cdot L_4 + L_1 \cdot B_z}.$$

simplify the denominator:

$$r \cdot \cos\phi \cdot L_1 + L_1 \cdot L_4 = r \cdot \cos\phi \cdot d + d \cdot L_4 + d \cdot B_z$$

$$r \cdot \cos\phi \cdot (L_1 - d) = L_4 \cdot (d - L_1) + d \cdot B_z = d \cdot B_z - L_4 \cdot (L_1 - d)$$

$$(r \cdot \cos\phi + L_4) \cdot (L_1 - d) = d \cdot B_z$$

$$r \cdot \cos\phi + L_4 = \frac{d \cdot B_z}{L_1 - d}. \tag{A4}$$

similarly, from (A2),

$$\begin{aligned} r \cdot \cos(\phi + \theta) + L_4 &= \frac{d \cdot B_z}{L_2 - d} \\ r \cdot \cos\phi \cdot \cos\theta - r \cdot \sin\phi \cdot \sin\theta + L_4 &= \frac{d \cdot B_z}{L_2 - d} \end{aligned} \tag{A5}$$

similarly, from (A3),

$$\begin{aligned} r \cdot \cos(\phi - \theta) + L_4 &= \frac{d \cdot B_z}{L_3 - d} \\ r \cdot \cos\phi \cdot \cos\theta + r \cdot \sin\phi \cdot \sin\theta + L_4 &= \frac{d \cdot B_z}{L_3 - d} \end{aligned} \tag{A6}$$

$$(4) * \cos \theta$$

$$r \cdot \cos\phi \cdot \cos\theta + L_4 \cdot \cos\theta = \frac{d \cdot B_z \cdot \cos\theta}{L_1 - d} \tag{A7}$$

adding (A5) and (A6) gives

$$2 \cdot r \cdot \cos\phi \cdot \cos\theta + 2 \cdot L_4 = \frac{d \cdot B_z}{L_2 - d} + \frac{d \cdot B_z}{L_3 - d}$$

transformation from (A7) gives

$$\begin{aligned} r \cdot \cos\phi \cdot \cos\theta &= \frac{d \cdot B_z \cdot \cos\theta}{L_1 - d} - L_4 \cdot \cos\theta \\ \left(\frac{2 \cdot d \cdot B_z \cdot \cos\theta}{L_1 - d} - 2 \cdot L_4 \cdot \cos\theta \right) + 2 \cdot L_4 &= \frac{d \cdot B_z}{L_2 - d} + \frac{d \cdot B_z}{L_3 - d} \\ 2 \cdot L_4 \cdot (1 - \cos\theta) &= \frac{d \cdot B_z}{L_2 - d} + \frac{d \cdot B_z}{L_3 - d} - \frac{2 \cdot d \cdot B_z \cdot \cos\theta}{L_1 - d} \\ L_4 &= \frac{\frac{d \cdot B_z}{L_2 - d} + \frac{d \cdot B_z}{L_3 - d} - \frac{2 \cdot d \cdot B_z \cdot \cos\theta}{L_1 - d}}{2 \cdot (1 - \cos\theta)} \end{aligned}$$

in addition, from (A1),

$$\begin{aligned} r \cdot \cos\phi + L_4 &= \frac{d \cdot B_z}{L_1 - d} \\ r \cdot \cos\phi &= \frac{d \cdot B_z}{L_1 - d} - L_4 \\ \cos \phi &= \frac{\frac{d \cdot B_z}{L_1 - d} - L_4}{r} \end{aligned} \tag{A8}$$

(A6) minus (A5) gives

$$\begin{aligned} 2 \cdot r \cdot \sin\phi \cdot \sin\theta &= \frac{d \cdot B_z}{L_3 - d} - \frac{d \cdot B_z}{L_2 - d} \\ r \cdot \sin\phi &= \frac{\frac{d \cdot B_z}{L_3 - d} - \frac{d \cdot B_z}{L_2 - d}}{2 \cdot \sin\theta} \end{aligned}$$

in addition, from (A8),

$$r^2 \cdot \cos^2 \phi + r^2 \cdot \sin^2 \phi = r^2 = \left(\frac{d \cdot B_z}{L_1 - d} - L_4 \right)^2 + \left(\frac{\frac{d \cdot B_z}{L_3 - d} - \frac{d \cdot B_z}{L_2 - d}}{2 \cdot \sin\theta} \right)^2$$

$$r = \sqrt{\left(\frac{d \cdot B_z}{L_1 - d} - L_4\right)^2 + \left(\frac{\frac{d \cdot B_z}{L_3 - d} - \frac{d \cdot B_z}{L_2 - d}}{2 \cdot \sin\theta}\right)^2}$$

Step II.

$$(B_x - B'_x)^2 + (B_y - B'_y)^2 = d^2 \tag{A9}$$

$$\frac{P_x - B'_x}{P_x - C'_x} = \frac{P_y - B'_y}{P_y - C'_y} = \frac{P_z - B'_z}{P_z - 0} \tag{A10}$$

$$\frac{P_x - B_x}{P_x - C_x} = \frac{P_y - B_y}{P_y - C_y} = \frac{P_z - B_z}{P_z - 0} \tag{A11}$$

$$\frac{Q_x - B'_x}{Q_x - D'_x} = \frac{Q_y - B'_y}{Q_y - D'_y} = \frac{Q_z - B'_z}{Q_z - 0} \tag{A12}$$

$$\frac{Q_x - B_x}{Q_x - D_x} = \frac{Q_y - B_y}{Q_y - D_y} = \frac{Q_z - B_z}{Q_z - 0} \tag{A13}$$

$$Q_x = P_x + r \cdot \sin\theta \tag{A14}$$

$$Q_y = P_y \tag{A15}$$

$$Q_z = P_z - \frac{r \cdot \sin\theta}{\tan\left(\frac{180-\theta}{2}\right)} \tag{A16}$$

$$B_z = B'_z \tag{A17}$$

derivations:

From (A10),

$$\frac{P_x - B'_x}{P_x - C'_x} = \frac{P_z - B'_z}{P_z}$$

$$P_x \cdot B'_z - P_z \cdot B'_x = C'_x \cdot (B'_z - P_z). \tag{A18}$$

from (A11),

$$\frac{P_x - B_x}{P_x - C_x} = \frac{P_z - B_z}{P_z}$$

$$P_x \cdot B_z - P_z \cdot B_x = C_x \cdot (B_z - P_z). \tag{A19}$$

(A18) minus (A19) gives

$$P_z \cdot (B_x - B'_x) = (P_z - B_z) \cdot (C_x - C'_x)$$

$$B_x - B'_x = \frac{(P_z - B_z) \cdot (C_x - C'_x)}{P_z}. \tag{A20}$$

from (A10),

$$\frac{P_y - B'_y}{P_y - C'_y} = \frac{P_z - B'_z}{P_z}$$

$$P_y \cdot B'_z - B'_y \cdot P_z = C'_y \cdot (B'_z - P_z). \tag{A21}$$

from (A11),

$$\frac{P_y - B_y}{P_y - C_y} = \frac{P_z - B_z}{P_z}$$

$$P_y \cdot B_z - B_y \cdot P_z = C_y \cdot (B_z - P_z). \tag{A22}$$

(A21) minus (A22) gives

$$P_z \cdot (B_y - B'_y) = (P_z - B_z) \cdot (C_y - C'_y)$$

$$B_y - B'_y = \frac{(P_z - B_z) \cdot (C_y - C'_y)}{P_z} \tag{A23}$$

substitute (A20) and (A12) into (A9):

$$\left[\frac{(P_z - B_z) \cdot (C_x - C'_x)}{P_z} \right]^2 + \left[\frac{(P_z - B_z) \cdot (C_y - C'_y)}{P_z} \right]^2 = d^2$$

$$(P_z - B_z)^2 \cdot [(C_x - C'_x)^2 + (C_y - C'_y)^2] = d^2 \cdot P_z^2$$

$$\left[(C_x - C'_x)^2 + (C_y - C'_y)^2 - d^2 \right] \cdot P_z^2 - 2 \cdot B_z \cdot [(C_x - C'_x)^2 + (C_y - C'_y)^2] \cdot P_z + [(C_x - C'_x)^2 + (C_y - C'_y)^2] \cdot B_z^2 = 0 \tag{A24}$$

Let

$$a = [(C_x - C'_x)^2 + (C_y - C'_y)^2 - d^2] \tag{A25}$$

$$b = -2 \cdot B_z \cdot [(C_x - C'_x)^2 + (C_y - C'_y)^2] \tag{A26}$$

$$c = [(C_x - C'_x)^2 + (C_y - C'_y)^2] \cdot B_z^2 \tag{A27}$$

substitute (A25), (A26), and (A27) into (A24):

$$a \cdot P_z^2 + b \cdot P_z + c = 0$$

$$P_z = \frac{-b \pm \sqrt{b^2 - 4 \cdot a \cdot c}}{2a}$$

where P_z is the larger value.

From (A12),

$$\frac{Q_x - B'_x}{Q_x - D'_x} = \frac{Q_z - B'_z}{Q_z}$$

$$Q_x \cdot B'_z - Q_z \cdot B'_x = (B'_z - Q_z) \cdot D'_x \tag{A28}$$

(A18) minus (A28) gives

$$(P_x - Q_x) \cdot B'_x - (P_z - Q_z) \cdot B'_x = C'_x \cdot (B'_z - P_z) - D'_x \cdot (B'_z - Q_z) \tag{A29}$$

substitute (A24) into (A29):

$$B'_x = \frac{D'_x \cdot (B'_z - Q_z) - C'_x \cdot (B'_z - P_z) - r \cdot \sin\theta \cdot B'_z}{P_z - Q_z}$$

from (A12),

$$\frac{Q_y - B'_y}{Q_y - D'_y} = \frac{Q_z - B'_z}{Q_z}$$

$$Q_y \cdot B'_y - Q_z \cdot B'_y = (B'_z - Q_z) \cdot D'_y \tag{A30}$$

(A21) minus (A30) gives

$$(P_y - Q_y) \cdot B'_z - (P_z - Q_z) \cdot B'_y = C'_y \cdot (B'_z - P_z) - D'_y \cdot (B'_z - Q_z). \quad (\text{A31})$$

we then find B'_y :

$$B'_y = \frac{C'_y \cdot (B'_z - P_z) - D'_y \cdot (B'_z - Q_z)}{Q_z - P_z}.$$

substitute B'_x into (A20):

$$B_x = B'_x + \frac{(P_z - B_z) \cdot (C_x - C'_x)}{P_z}.$$

substitute B'_y into (A23):

$$B_y = B'_y + \frac{(P_z - B_z) \cdot (C_y - C'_y)}{P_z}.$$

substitute B'_x into (A18):

$$P_x = \frac{P_z \cdot B'_x + C'_x \cdot (B'_z - P_z)}{B'_z}.$$

substitute B'_y into (A21):

$$P_y = \frac{P_z \cdot B'_y + C'_y \cdot (B'_z - P_z)}{B'_z}.$$

References

1. Fava, L.; Dummer, P. Periapical radiographic techniques during endodontic diagnosis and treatment. *Int. Endod. J.* **1997**, *30*, 250–261. [[CrossRef](#)]
2. Vandenberghe, B.; Jacobs, R.; Bosmans, H. Modern dental imaging: A review of the current technology and clinical applications in dental practice. *Eur. Radiol.* **2010**, *20*, 2637–2655. [[CrossRef](#)] [[PubMed](#)]
3. Fu, H.-M.; Chueh, H.-S.; Tsai, W.-K.; Chen, J.-C.J.B.E.A. Development and evaluation of reconstruction methods for an in-house designed cone-beam micro-CT imaging system. *Biomed. Eng. Appl. Basis Commun.* **2006**, *18*, 270–275. [[CrossRef](#)]
4. Kiljunen, T.; Kaasalainen, T.; Suomalainen, A.; Kortensniemi, M. Dental cone beam CT: A review. *Physica Med.* **2015**, *31*, 844–860. [[CrossRef](#)] [[PubMed](#)]
5. Pauwels, R.; Araki, K.; Siewerdsen, J.; Thongvigitmanee, S. Technical aspects of dental CBCT: State of the art. *Dentomaxillofacial Radiol.* **2014**, *44*, 20140224. [[CrossRef](#)] [[PubMed](#)]
6. Metsälä, E.; Henner, A.; Ekholm, M. Quality assurance in digital dental imaging: A systematic review. *Acta Odontol. Scand.* **2014**, *72*, 362–371. [[CrossRef](#)]
7. Patel, S.; Dawood, A.; Whaites, E.; Pitt Ford, T. New dimensions in endodontic imaging: Part 1. Conventional and alternative radiographic systems. *Int. Endod. J.* **2009**, *42*, 447–462. [[CrossRef](#)]
8. Liao, C.-W.; Hsieh, C.-J.; Huang, H.-L.; Fuh, L.-J.; Kuo, C.-W.; Lin, Y.-b.; Chen, J.-C.; Hsu, J.-T.J.B.E.A. Prototype of a 2.5 D periapical radiography system using an intraoral computed tomosynthesis approach. *Biomed. Eng. Appl. Basis Commun.* **2018**, *30*, 1850004. [[CrossRef](#)]
9. Shan, J.; Tucker, A.; Gaalaas, L.; Wu, G.; Platin, E.; Mol, A.; Lu, J.; Zhou, O.J.D.R. Stationary intraoral digital tomosynthesis using a carbon nanotube X-ray source array. *Dentomaxillofacial Radiol.* **2015**, *44*, 20150098. [[CrossRef](#)]
10. Inscoe, C.R.; Wu, G.; Soulioti, D.E.; Platin, E.; Mol, A.; Gaalaas, L.R.; Anderson, M.R.; Tucker, A.W.; Boyce, S.; Shan, J. Stationary intraoral tomosynthesis for dental imaging. In Proceedings of the Medical Imaging 2017: Physics of Medical Imaging, Orlando, FL, USA, 13–16 February 2017; p. 1013203.
11. Inscoe, C.R.; Platin, E.; Mauriello, S.M.; Broome, A.; Mol, A.; Gaalaas, L.R.; Regan Anderson, M.W.; Puett, C.; Lu, J.; Zhou, O.J.M.p. Characterization and preliminary imaging evaluation of a clinical prototype stationary intraoral tomosynthesis system. *Med. Phys.* **2018**, *45*, 5172–5185. [[CrossRef](#)]

12. Liao, C.-W.; Huang, K.-J.; Chen, J.-C.; Kuo, C.-W.; Wu, Y.-Y.; Hsu, J.-T. A Prototype Intraoral Periapical Sensor with High Frame Rates for a 2.5 D Periapical Radiography System. *Appl. Bionics Biomech.* **2019**, *2019*. [[CrossRef](#)] [[PubMed](#)]
13. Xiang, Q.; Wang, J.; Cai, Y. A geometric calibration method for cone beam CT system. In Proceedings of the Eighth International Conference on Digital Image Processing (ICDIP 2016), Chengdu, China, 20–22 May 2016; p. 100333G.
14. Zhao, J.; Hu, X.; Zou, J.; Hu, X.J.S. Geometric parameters estimation and calibration in cone-beam micro-CT. *Sensor* **2015**, *15*, 22811–22825. [[CrossRef](#)] [[PubMed](#)]
15. Johnston, S.M.; Johnson, G.A.; Badea, C.T.J.M.p. Geometric calibration for a dual tube/detector micro-CT system. *Med. Phys.* **2008**, *35*, 1820–1829. [[CrossRef](#)]
16. Von Smekal, L.; Kachelrieß, M.; Stepina, E.; Kalender, W.A.J.M.p. Geometric misalignment and calibration in cone-beam tomography: Geometric misalignment and calibration in cone-beam tomography. *Med. Phys.* **2004**, *31*, 3242–3266. [[CrossRef](#)] [[PubMed](#)]
17. Li, L.; Yang, Y.; Chen, Z.J.O.E. Geometric estimation method for x-ray digital intraoral tomosynthesis. *Opt. Eng.* **2016**, *55*, 063105. [[CrossRef](#)]
18. Richard, L.; Webber, W.-S. Self-calibrated tomosynthetic, radiographic-imaging system, method, and device. U.S. Patent No 5,359,637, 25 October 1994.
19. Yang, Y.; Li, L.; Chen, Z.; Chang, M. Geometrical calibration method for x-ray intra-oral digital tomosynthesis. In Proceedings of the 2014 IEEE Nuclear Science Symposium and Medical Imaging Conference (NSS/MIC), Seattle, WA, USA, 8–15 November 2014; pp. 1–4.
20. Li, L.; Chen, Z.; Zhao, Z.; Wu, D. X-ray digital intra-oral tomosynthesis for quasi-three-dimensional imaging: System, reconstruction algorithm, and experiments. *Opt. Eng.* **2013**, *52*, 013201. [[CrossRef](#)]
21. Sato, K.; Ohnishi, T.; Sekine, M.; Haneishi, H. Geometry calibration between X-ray source and detector for tomosynthesis with a portable X-ray system. *Int. J. Comput. Assisted Radiol. Surg.* **2017**, *12*, 707–717. [[CrossRef](#)]
22. Miao, H.; Wu, X.; Zhao, H.; Liu, H. A phantom-based calibration method for digital x-ray tomosynthesis. *J. X-Ray Sci. Technol.* **2012**, *20*, 17–29. [[CrossRef](#)]
23. Chtcheprov, P.; Hartman, A.; Shan, J.; Lee, Y.Z.; Zhou, O.; Lu, J. Optical geometry calibration method for free-form digital tomosynthesis. In Proceedings of the Medical Imaging 2016: Physics of Medical Imaging, San Diego, CA, USA, 27 February–3 March 2016; p. 978365.
24. Fayad, M.I.; Nair, M.; Levin, M.D.; Benavides, E.; Rubinstein, R.A.; Barghan, S.; Hirschberg, C.S.; Ruprecht, A. AAE and AAOMR joint position statement: Use of cone beam computed tomography in endodontics 2015 update. *Oral Surg. Oral Med. Oral Pathol. Oral Radiol.* **2015**, *120*, 508–512. [[CrossRef](#)]
25. Hayakawa, Y.; Yamamoto, K.; Kousuge, Y.; Kobayashi, N.; Wakoh, M.; Sekiguchi, H.; Yakushiji, M.; Farman, A. Clinical validity of the interactive and low-dose three-dimensional dento-alveolar imaging system, Tuned-Aperture Computed Tomography. *Bull. Tokyo Dent. Coll.* **2003**, *44*, 159–167. [[CrossRef](#)]
26. Groenhuis, R.A.; Webber, R.L.; Ruttimann, U.E.J.O.S. Computerized tomosynthesis of dental tissues. *Oral Med. Oral Pathol.* **1983**, *56*, 206–214. [[CrossRef](#)]
27. Grant, D.G. Tomosynthesis: A three-dimensional radiographic imaging technique. *IEEE Trans. Biomed. Eng.* **1972**, *1*, 20–28. [[CrossRef](#)] [[PubMed](#)]
28. Ziegler, C.M.; Franetzki, M.; Denig, T.; Muhling, J.; Hassfeld, S. Digital tomosynthesis-experiences with a new imaging device for the dental field. *Clin. Oral Investig.* **2003**, *7*, 41–45. [[CrossRef](#)] [[PubMed](#)]
29. Rashedi, B.; Tyndall, D.A.; Ludlow, J.B.; Chaffee, N.R.; Guckes, A. Tuned aperture computed tomography (TACT[®]) for cross-sectional implant site assessment in the posterior mandible. *J. Prosthodontics* **2003**, *12*, 176–186. [[CrossRef](#)]
30. Harase, Y.; Araki, K.; Okano, T. Diagnostic ability of extraoral tuned aperture computed tomography (TACT) for impacted third molars. *Oral Surg. Oral Med. Oral Pathol. Oral Radiol. Endodontol.* **2005**, *100*, 84–91. [[CrossRef](#)] [[PubMed](#)]
31. Limrachtamorn, S.; Edge, M.; Gettleman, L.; Scheetz, J.; Farman, A. Array geometry for assessment of mandibular implant position using tuned aperture computed tomography (TACT[™]). *Dentomaxillofacial Radiol.* **2004**, *33*, 25–31. [[CrossRef](#)] [[PubMed](#)]

32. Harase, Y.; Araki, K.; Okano, T. Accuracy of extraoral tuned aperture computed tomography (TACT) for proximal caries detection. *Oral Surg. Oral Med. Oral Pathol. Oral Radiol. Endodontol.* **2006**, *101*, 791–796. [[CrossRef](#)]
33. Yang, K.; Kwan, A.L.; Miller, D.F.; Boone, J. A geometric calibration method for cone beam CT systems. *Med. Phys.* **2006**, *33*, 1695–1706. [[CrossRef](#)]
34. Sun, Y.; Hou, Y.; Zhao, F.; Hu, J. A calibration method for misaligned scanner geometry in cone-beam computed tomography. *NDT E Int.* **2006**, *39*, 499–513. [[CrossRef](#)]
35. Wang, X.; Mainprize, J.G.; Kempston, M.P.; Mawdsley, G.E.; Yaffe, M.J. Digital breast tomosynthesis geometry calibration. In *Proceedings of the Medical Imaging 2007: Physics of Medical Imaging*, San Diego, CA, USA, 18–22 February 2007; p. 65103B.
36. Claus, B.E.H.; Opsahl-Ong, B.; Yavuz, M. Method, apparatus, and medium for calibration of tomosynthesis system geometry using fiducial markers with non-determined position. U.S. Patent No. 6,888,924, 3 May 2005.



© 2020 by the authors. Licensee MDPI, Basel, Switzerland. This article is an open access article distributed under the terms and conditions of the Creative Commons Attribution (CC BY) license (<http://creativecommons.org/licenses/by/4.0/>).